PAPER

Check for updates

Nanozyme colorimetric sensor array-based Au as an electron bank facilitated surface charge redistribution of CeO₂ for on-site detection and discrimination of sulfur-containing metal salts†

Yang Song,[a] Zhongyuan Gu,[a] Hao Wang,[a] Xinxin Shi,[b] Changchun He,[a] Tongxiang Li,[b] Yan Chen,*[a] Zhao Li 🄳 *[a] and Lin Tian 🄳 *[a,b]

Developing a highly efficient array-based sensing platform for sulfur-containing metal salt (SCM) analysis is imperious due to its potential to harm the environment and human health. Herein, we fabricated a ternary channel colorimetric sensor array technique to monitor multiple SCMs simultaneously, depending on the Au nanoparticle-loaded CeO₂ nanobelt (Au/CeO₂) heterostructure with excellent peroxidase-like (POD-like) activity. The results of XPS and DFT calculations revealed that Au NPs as an electron bank can promote the charge redistribution on the surface of CeO₂. This process increases the ratio of Ce^{3+}/Ce^{4+}, facilitates the release of OH* and the desorption of H₂O, and significantly enhances the POD-like activity. Subsequently, colorimetry- and sensor array-based Au/CeO₂ was developed, in integrating diverse degrees of TMB oxidation, owing to their various catalysis behaviors, leading to distinct patterns as "fingerprints" for different SCMs. The gained distinct patterns were recognized and processed *via* principal component analysis (PCA), enabling specific and sensitive identification and discrimination of different concentrations of SCMs with a detection limit of 5 μM. To advance the field determination of various SCM concentrations, we creatively constructed a portable smartphone device-based autonomous sensing platform with a linear range of 5–110 μM, which further indicates the potential utility of colorimetric sensor arrays. This work opens new avenues for efficient on-site SCM detection and discrimination by enhancing the POD-like activity of CeO₂ through surface electron redistribution.

1 Introduction

Sulfur-containing metal salts (SCMs), such as sodium sulfide (Na₂S), sodium sulfite (Na₂SO₃) and sodium persulfate (Na₂S₂O₈), pose potential risks to the health of both humans and animals as they can enter the food chain through water or environmental pathways.[1–4] Apparently, excessive intake of SCMs may directly result in several illnesses such as nervous system disorder, diabetes, tumor and so forth.[5–7] Therefore, it is crucial to construct a reliable and sensitive method for the simultaneous environmental analysis of the above SCMs.

Several technologies have been developed for the qualitative and quantitative detection of SCMs, including high-performance liquid chromatography (HPLC),[8,9] chemiluminescence (CL),[10,11] electrochemical (EC) methods,[12] fluorescence spectroscopy (FL),[13,14] surface-enhanced Raman scattering (SERS),[15] *etc*. However, these technologies possess some drawbacks such as tedious sample pretreatment, high cost, long-time measurements, professional operator, and clumsy instruments and equipment, which in turn greatly limits their application for on-site and portable detection. The literature also revealed that the specific probe employed in sensitive and rapid approaches are toxic organic compounds and easily inactivated.[16] In this regard, colorimetric sensing platforms have obtained wide interest because of their simple operation, easy sample treatments, quick signal readout, low cost, *etc*.[17–19] Unfortunately, the traditional colorimetry sensing platform, hindered by the "lock-key" selective recognition and detection mechanism, can only be utilized to monitor or identify a single SCM substance. Hence, it is of great significance and urgent need to develop a quick, simple, low-cost, and sensitive

[a] School of Materials and Chemical Engineering, Xuzhou University of Technology, Xuzhou 221018, PR China. E-mail: chenyan@xzit.edu.cn, xzitlz@xzit.edu.cn, xzittl@xzit.edu.cn

[b] School of Food (Biology) Engineering, Xuzhou University of Technology, Xuzhou 221018, PR China. E-mail: litx@xzit.edu.cn

† Electronic supplementary information (ESI) available. See DOI: https://doi.org/10.1039/d5nr01503k

technology for the on-site and simultaneous detection of multiple SCMs in the actual application.

Strikingly, inspired by mammalian olfaction, the colorimetric sensor array utilizes a non-selective recognition component to produce a composite signal pattern, serving as a distinct fingerprint for each analyte. This approach breaks free from the constraints of the traditional "lock-key" selective recognition and detection mechanism.[20] Moreover, they can identify various analytes with similar structures and properties and provide merits such as a visual sensing platform, simple operation, and determination of multiple analytes simultaneously *via* multivariate statistical methods.[21] In general, the colorimetric sensor array system comprises different colorimetric indicators such as nanozyme-based catalysts,[22,23] thermal indicators, dyes, and so forth, which are cross-reactive to diverse chemical analysts, and further offers analyte-selective color change patterns. At present, there are some literature studies on utilizing colorimetric sensor arrays for the simultaneous determination of molecular analytes by boosting the sensitivity of the indicators.[24]

The utilization of nanozymes, one kind of nanomaterial with multiple enzyme-like catalytic capabilities, has become a promising strategy to construct various colorimetric sensing platforms.[25] Nanozymes have the merits of low storage cost, high catalytic activity under weakly acidic conditions, and simple and large-scale preparation and are widely utilized in analytical detection, biomedicine, and biosensing in comparison with natural enzymes.[26] To date, there have been many reports on bimetallic nanomaterials and single atom catalysts and because of the unique structural traits, they possess a more outstanding enzyme-mimicking catalytic activity.[27–29] Among the numerous nanozyme materials, metallic oxides such as CeO_2 are known for their high nanozyme catalytic activities and unique structures.[30] They have attracted increasing interest to substitute natural enzymes. However, the low content of Ce^{3+} in CeO_2 is not conducive to the improvement of enzyme-like activity. Therefore, it is necessary to introduce a metal with good electron transport performance as an electronic pump to promote the surface charge redistribution of CeO_2 and increase the ratio of Ce^{3+}/Ce^{4+}.[31] Notably, nanozyme-based colorimetric sensor arrays based on monatomic alloys are used for the discrimination of SCMs.[32] However, few research studies on the construction of sensor arrays by integrating nanozyme colorimetric metallic oxide materials with interface engineering have been reported. Furthermore, the catalytic reaction mechanism occurring on the surface of nanozyme materials remains unclear.

Here, instead of utilizing the classical sensing method, we constructed Au/CeO_2 for the simultaneous identification and discrimination of SCM substances (Na_2S, Na_2SO_3 and $Na_2S_2O_8$) based on the pattern recognition response. First, Au with rich surface charge and good conductivity is introduced to the CeO_2 surface as an electron bank to form a Au/CeO_2 heterojunction. Then, the specificity and sensitivity of the sensor array were detected by highly efficient POD-like activity of the heterostructure Au/CeO_2 nanozyme under the optimized

experimental conditions and with diverse interactions of various SCMs on oxTMB *via* principal component analysis (PCA) and colorimetric sensing systems. Upon using the heterostructure Au/CeO_2 nanozyme, TMB was directly oxidized with the addition of H_2O_2. Subsequently, the colorimetric sensor array (3 SCMs × 1 channel × 6 replicates) was successfully fabricated. In addition, by keeping in mind the growing demand for portable devices for on-site identification of SCMs, an intelligent smartphone has also been employed for SCM detection. Mechanism study showed that Au NPs as an electron bank can promote the charge redistribution on the surface of CeO_2, which can increase the ratio of Ce^{3+}/Ce^{4+}, facilitate the release of OH* and the desorption of H_2O, and significantly improve the POD-like activity.

2 Experimental section

2.1 Chemicals

The detailed chemicals and instrumentation can be seen in the ESI.†

2.2 Preparation of Au/CeO₂

Preparation method of CeO₂. In a 30 °C water bath, 5.56 g $Ce(NO_3)_2·6H_2O$ and 4.0 g NH_4HCO_3 were separately dissolved in 200 mL of deionized water. The NH_4HCO_3 solution was rapidly added to the $Ce(NO_3)_2·6H_2O$ solution while maintaining the same temperature, followed by stirring for 0.5 h and then allowing it to stand at 30 °C for 24 hours. The crude products were filtered, washed with deionized water and anhydrous ethanol separately, and dried at 60 °C before ultimately synthesizing nanobelt CeO_2 through annealing at a temperature of 450 °C for four hours.

Preparation of Au/CeO₂. The CeO_2 nanobelt (25 mg) was dispersed in 5 mL of deionized water. Subsequently, the $HAuCl_4$ solution (0.02 g mL^{-1}) was injected into the CeO_2 dispersion solution (0.5 mL) under vigorous stirring conditions and stirred vigorously for 12 hours. The resulting mixture was then subjected to vacuum filtration to collect the solid, followed by multiple washes with deionized water and drying at 80 °C. Finally, the products were obtained by annealing at 200 °C under an air atmosphere for 1 h.

2.3 Peroxidase-like activity of Au/CeO₂

Peroxidase-like catalytic activities of the nanomaterial-based nanozymes were commonly investigated by steady-state kinetics tests. In general, tests were carried out utilizing TMB as a typical catalytic substrate at 25 °C in a 96-well plate. The data were recorded by using a microplate reader at 652 nm. A 0.1 M HAc–NaAc buffer solution (pH 4.5) was utilized as the reaction solution, and 100 μg mL^{-1} Au/CeO_2 was utilized for its steady-state kinetics test. The heterostructure Au/CeO_2 nanozymes were mixed with a series of TMB concentrations in the HAc–NaAc buffer solution, and the absorbance intensity of the reaction system at 652 nm was quickly recorded by using a microplate reader. Subsequently, the "absorbance intensity *versus*

time" curve was acquired, which could be utilized to calculate the initial reaction velocity (V). Finally, the kinetics constants including V_{max} and K_m were acquired by fitting the reaction velocity values and the TMB concentrations based on the Michaelis–Menten equation as follows:

$$\frac{1}{V} = \frac{1}{V_{max}} + \frac{K_m}{V_{max}} \times \frac{1}{[S]}$$

where V represents the initial reaction velocity, and V_{max} and K_m represent the maximum reaction rate and Michaelis–Menten constant, respectively. [S] represents the concentration of the TMB substrate.

2.4 Sensor array preparation

The colorimetric sensor array analysis for SCM detection was designed using the [Au/CeO$_2$ + TMB/H$_2$O$_2$] reaction system. First, 150 μL of Au/CeO$_2$ (1.0 mg mL^{-1}) was added into 2850 μL of HAc–NaAc buffer solution buffer (0.1 M, pH 4.5) including 1 mM TMB and 10 mM H$_2$O$_2$ and mixed together at 25 °C. Then, the above solution was divided into two groups. To the control group, 5 μL of water was added into the above reaction solution, and mixed thoroughly. To the experimental group, 5 μL of analyte SCMs (Na$_2$S, Na$_2$SO$_3$ and Na$_2$S$_2$O$_8$) with different concentrations were added into the similar reaction solutions under the optimal analytical conditions. After incubating for 5 min, the absorbance response at 652 nm was collected and recorded by using a portable microplate reader. Each SCM analysis was carried out by six repetitions. Accordingly, three kinds of SCMs were analyzed six times on the colorimetric sensor array comprising Au/CeO$_2$ nanozymes, offering training data for the 3 SCMs × 1 channel × 6 replicates. Finally, all the data analyses were conducted utilizing Origin 22.0; in all cases, PCA was performed on the original data matrix utilizing the minimum variance for recognition.

2.5 Density functional theory (DFT) calculations

Spin polarization DFT calculations were performed using the Vienna *ab initio* simulation package (VASP) code. The projector augmented wave method (PAW) and the Perdew–Burke–Ernzerhof (PBE) exchange correlation functional were performed to describe the valence electron and core interactions. A plane wave basis set was employed with the kinetic cut-off energy of 500 eV. All structures were fully optimized until the energy and residual force converged to 10^{-5} eV and 0.03 eV Å^{-1}. The DFT-D3 method was utilized to estimate the adsorption strength accurately. The vacuum layer of 15 Å was set. A 3 × 3 × 1 Monkhorst–Pack grid was sampled.
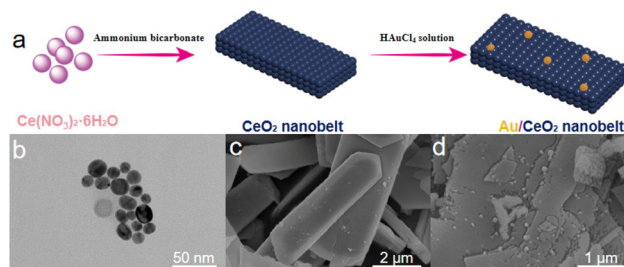
The adsorption energy was defined as:

$$E = E_{[total]} - (E_{[mol]} + E_{[slab]}) \tag{1}$$

where E is the adsorption energy, $E_{[mol]}$ is the energy of the molecule, $E_{[slab]}$ is the energy of the slab and $E_{[total]}$ is the total energy of the molecule adsorbed on the slab.
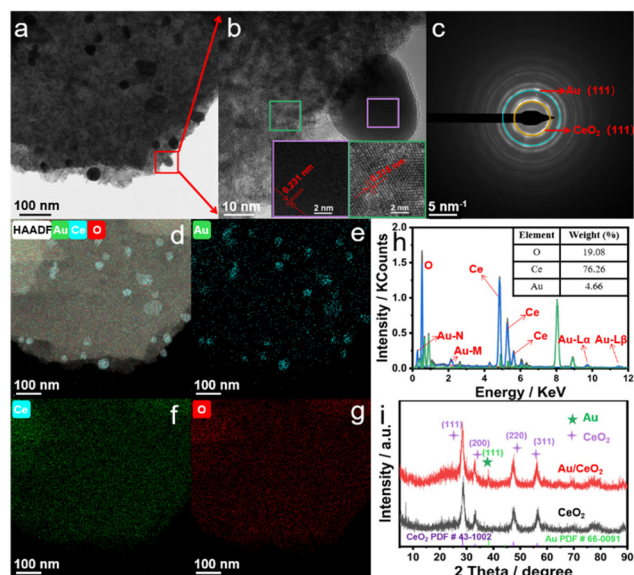
3 Results and discussion

3.1 Characterization of Au/CeO$_2$

As depicted in Fig. 1a, the preparation process of Au/CeO$_2$ was fully described in detail. The Au NP solution was firstly characterized *via* TEM. It was clear that the Au nanoparticle showed a spherical shape with a size of 10–20 nm (Fig. 1b). The morphology of Au/CeO$_2$ was firstly characterized *via* SEM. It was clear that the crude CeO$_2$ primarily consisted of nanobelts (NBs) with a width of about 2 μm (Fig. 1c), and the Au modification did not remarkably affect its original structure (Fig. 1d). The Au/CeO$_2$ NBs displayed many significant sphere-like nanoparticles on surfaces, while the pure CeO$_2$ NBs were nearly smooth. This phenomenon could have been ascribed to the surface doping of Au nanoparticles. Then, TEM was utilized to further characterize the morphology. Fig. 2a shows the TEM image of Au/CeO$_2$ NBs; it was clear that the Au nanoparticle successfully loaded on CeO$_2$. The obvious nanostructure can also be clearly seen in Fig. 2b, which is distinguished in the green and purple rectangular areas. The lattice spacing of 0.231 and 0.315 nm shown in Fig. 2b could be assigned to the (111) plane of Au and CeO$_2$, which was matched well with the bright ring consisting of discrete spots in the selected area electron diffraction (SAED) image of different areas in Fig. 2c, corresponding to the red rectangular area in Fig. 2a. The HAADF-STEM and corresponding elemental mapping images (Fig. 2d–g) of Au/CeO$_2$ NBs suggested the homogeneous distribution of the Au, Ce, and O elements throughout the entire NBs surfaces, which also depicted the significant heterostructure. EDS showed that the atomic number ratio of Au, Ce, and O was about 4.66 : 76.26 : 19.08 (Fig. 2h). In order to investigate the crystal phase of different products, XRD was performed. Fig. 2i shows the typical XRD patterns of various products. All the characteristic peaks were well corresponded to Au (PDF # 66-0091) and CeO$_2$ (PDF # 43-1002),[33,34] respectively. Notably, the characterization peak around 38.1° was pointed to the (111) crystal plane of Au, and the peaks around 28.4°, 32.9°, 47.3°, 56.2° were assigned to the (111), (200), (220), and (311) crystal planes of CeO$_2$, respectively. After a detailed observation, we could find that some peaks were slightly shifted in comparison with the standard peaks including the (111) crystal plane of CeO$_2$.

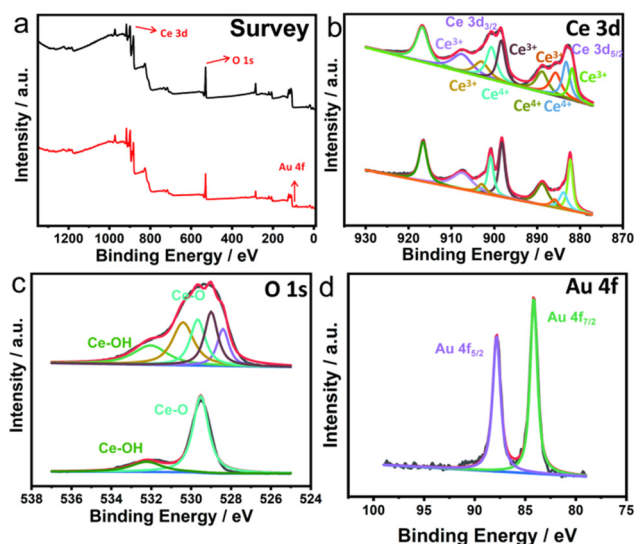**Fig. 1** (a) Schematic illustration of the preparation procedure of the Au/CeO$_2$ NB heterostructure. SEM images of (b) Au, (c) CeO$_2$ and (d) Au/CeO$_2$.

Fig. 2 (a) TEM image of the Au/CeO₂ NB heterostructure. (b) HRTEM images; the rectangular areas represent the FFT patterns of the selected areas (green and purple boxes), (c) SAED pattern of the different areas, and (d) STEM image and the corresponding elemental mapping images of (e) Au, (f) Ce, and (g) O in Au/CeO₂. (h) The EDS spectrum and (i) XRD pattern of the Au/CeO₂ heterostructure.

Furthermore, the surface elements and valence states of Au/CeO₂ were characterized utilizing XPS. As shown in Fig. 3a, the survey spectra of Au/CeO₂ display the XPS peaks of Au 4f, O 1s and Ce 3d, establishing that the Au NPs were successfully loaded into the surface of CeO₂ nanobelts. Fig. 3b displays five signal peaks of CeO₂ at 882.3, 886.0, 898.2, 903.0, and 907.6 eV, which were assigned to Ce $3d_{5/2}$ and Ce $3d_{3/2}$ of Ce³⁺.[35,36] In addition, four characteristic peaks at 883.9, 888.9, 900.8 and
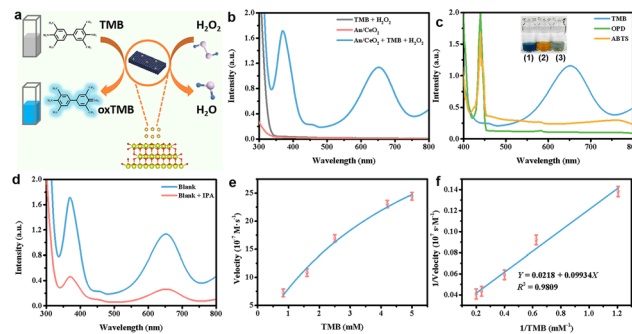
916.6 eV were attributed to Ce⁴⁺ for Ce $3d_{5/2}$ and Ce $3d_{3/2}$.[37] Compared with CeO₂, Au/CeO₂ showed a similar XPS pattern. In general, the higher the ratio of Ce³⁺/Ce⁴⁺, the higher the POD-like catalytic activity.[38] Through calculation, it was found that the ratio of Ce³⁺/Ce⁴⁺ in Au/CeO₂ was 1.1, which exceeded that in CeO₂ by 0.2. This suggests that Au/CeO₂ may possess enhanced POD-like catalytic activity. For the O 1s of Au/CeO₂ (Fig. 3d), two peaks at 529.5 and 532.2 eV were ascribed to the Ce–O and Ce–OH bonds, respectively. The O1s of CeO₂ showed abundant peaks assigned to the Ce–O. C–O, and O–H bonds, implying that CeO₂ was more hydrophilic than Au/CeO₂.[39] Fig. 3c shows the Au 4f spectrum of Au/CeO₂. As observed, the characteristic peaks at 84.1 and 87.8 eV corresponded to Au $4f_{7/2}$ and Au $4f_{5/2}$, respectively.[40] From the foregoing analysis, it was evident that the incorporation of Au NPs induces an electron redistribution within CeO₂, resulting in an increased ratio of Ce³⁺ and decreased hydrophilicity. Notably, XPS analysis revealed that Ce⁴⁺ in the CeO₂ nanocrystals and the introduction of Au generate a polar Ce⁴⁺–O–Au interface. These results demonstrated that Au/CeO₂ nanocrystals were composed of a CeO₂ core, a Ce⁴⁺–O–Au heterointerface, and highly strained Au islands.

3.2 Au/CeO₂ nanozymes mimicking peroxidase activity

After proving the successful preparation of Au/CeO₂, the enzyme-like catalytic capability of Au/CeO₂ was investigated by utilizing TMB as a typical chromogenic substrate. Among the as-prepared pure Au nanoparticles, CeO₂ nanobelts and Au/CeO₂ nanocomposites, Au/CeO₂ exhibited the strongest peroxidase-like catalytic activity. Thus, Au/CeO₂ was utilized as an example to explore their peroxidase-like catalytic activity by detecting the catalytic oxidation of a common peroxidase chromogenic substrate colorless TMB *via* UV-Vis absorption spectroscopy (Fig. 4a). As depicted in Fig. 4b, the [Au/CeO₂ + TMB/

Fig. 3 (a) XPS survey spectra of Au/CeO₂. The high-resolution XPS spectra of (b) Ce 3d, (c) Au 4f, and (d) O1s of Au/CeO₂.

Fig. 4 (a) Schematic illustration of the catalytic reaction of the oxidase-like capability of Au/CeO₂. (b) UV-Vis absorption spectra of various reaction systems. (c) UV-Vis absorption spectra of 1 mM TMB, 2 mM OPD, and 1 mM ABTS after catalyzing oxidation with Au/CeO₂. Inset: the corresponding figures exhibiting the visual color changes of (1) TMB, (2) OPD, and (3) ABTS in the [Au/CeO₂ + TMB//H₂O₂] reaction system. (d) UV-Vis absorption spectra of Au/CeO₂-mediated TMB oxidation in the absence and presence of IPA. (e) The Michaelis–Menten curve of Au/CeO₂ with TMB. (f) Double-reciprocal plot of Au/CeO₂ with a series of TMB concentrations.
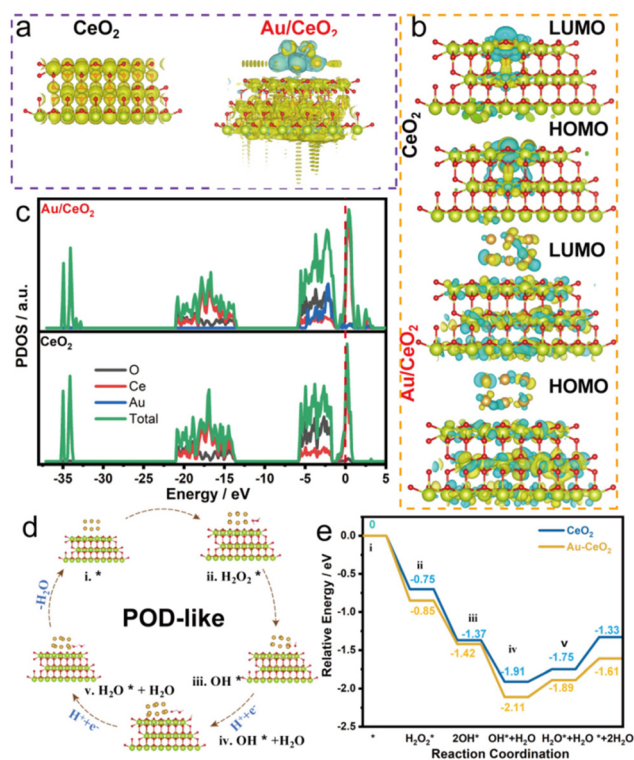
H_2O_2] reaction system produced a light-blue-colored oxidation product with an obvious absorption response located at 652 nm, suggesting the outstanding peroxidase-like catalytic capability of Au/CeO_2. In addition to the common TMB chromogenic substrate, two other common oxidase substrates including ABTS and OPD were also employed to further demonstrate the peroxidase-like catalytic capability of Au/CeO_2. As displayed in Fig. 4c, Au/CeO_2 could also generate a characterization green-colored oxidation ABTS product and a typical yellow color for the oxidized OPD with a significant absorption signal. The above results suggested that the [Au/CeO_2 + TMB/H_2O_2] reaction system had a strong adsorption response because of the presence of the corresponding oxidation products, demonstrating that Au/CeO_2 could catalyze the oxidation of common chromogenic substrates with excellent peroxidase-like catalytic activity with the addition of H_2O_2. To further explore the catalytic mechanism in the [Au/CeO_2 + TMB/H_2O_2] reaction system on the oxidation and color change of TMB, 200 L of isopropyl alcohol (IPA, served as the $^\bullet$OH scavenger) was added into the above mixture solution. As seen in Fig. 4d, the absorption intensity at 652 nm was remarkably decreased in the presence of IPA, suggesting that TMB was oxidized to oxTMB. This result demonstrated the consumption of OH by IPA, leading to the incomplete oxidation of TMB. Thus, OH played a crucial role toward the TMB oxidation procedure in the [Au/CeO_2 + TMB/H_2O_2] reaction system. Meanwhile, we further performed a typical quenching assay to investigate the effect of ROS on peroxidase-like activity. Sodium azide (NaN_3), 1,4-benzoquinone (BQ), and IPA, the classical scavengers for $^\bullet$OH, $O_2^{\bullet-}$ and singlet oxygen, were utilized to explore their influences on catalytic activity (Fig. S1†). As depicted in Fig. S1,† the introduction of each IPA and BQ caused remarkable change on the peroxidase-like catalytic activity, suggesting that $^\bullet$OH and $O_2^{\bullet-}$ may be the important species participating in the oxidation of TMB. To quantify the catalytic efficiency of Au/CeO_2, its peroxidase-like activity was analyzed by utilizing a typical steady-state kinetic test. As seen in Fig. 4e, the catalytic kinetics of the oxidation of the Au/CeO_2 nanozyme was mainly related to the concentration of the TMB, which was also well fitted to the typical Michaelis–Menten curve and the Lineweaver–Burk plot of enzyme catalytic reactions. The kinetic parameters of the maximum initial velocity (V_{max}) and Menten constant (K_m) were calculated to be 2.55×10^{-7} M s^{-1} and 0.77 mM, respectively. Meanwhile, the Au/CeO_2 nanozyme displayed a V_{max} value for 2.95×10^{-7} M s^{-1} for H_2O_2 (Fig. 4f). Based on the above results of the kinetic parameters, Au/CeO_2 displayed POD-like activity superior to that of horseradish peroxidase (HRP) and the most reported nanozymes, demonstrating that Au/CeO_2 possessed potential as a substitute for natural enzymes.

To achieve the optimal analytical performance of the colorimetric sensor array, some limiting parameters including reaction time, Au percentage, pH values, concentration of TMB and Au/CeO_2 were also optimized. As depicted in Fig. S2,† the peroxidase-like catalytic activity of the Au/CeO_2 nanozyme decreased significantly by varying the pH from 4.0 to 8.0.

Clearly, the maximum peroxidase-like activity was realized at pH 4.5 for Au/CeO_2. Meanwhile, the optimal experimental conditions were 0.5%Au/CeO_2, 10 mM H_2O_2, 1 mM TMB and 50 μg mL^{-1} Au/CeO_2 for 10 min.

3.3 Mechanism study of POD-like catalytic activity

To further elucidate the enhanced catalytic performance of the Au/CeO_2 nanocatalyst, density functional theory (DFT) calculations were conducted to investigate the underlying action mechanism.[41] The complete geometric configurations of CeO_2 and Au/CeO_2, optimized for a monoclinic lattice, are depicted in Fig. 5a. The charge density difference plot reveals that CeO_2 maintains a uniformly dispersed electron cloud across the structure in a stable state, whereas Au/CeO_2 exhibits a concentrated electron cloud density surrounding CeO_2, suggesting that the introduction of Au NPs induces electron redistribution on the CeO_2 surface. The influence of Au NPs on the electronic configuration of CeO_2 was then examined via the lowest unoccupied molecular orbital (LUMO) and highest occupied molecular orbital (HOMO) calculations for both CeO_2 and Au/CeO_2. As illustrated in Fig. 5b, the LUMO and HOMO levels of CeO_2 were 2.24 and −0.07 eV, respectively, while those of Au/CeO_2 were 2.13 and 1.22 eV, respectively. Furthermore, the energy gap of Au/CeO_2 (0.91 eV) was narrower than that of CeO_2 (2.31

Fig. 5 (a) Charge density difference illustration of CeO_2 and Au/CeO_2. (b) HOMO–LUMO energy levels and the interfacial diagrams of the molecular orbitals for CeO_2 and Au/CeO_2. (c) Density of states of CeO_2 and Au/CeO_2. (d) Proposed reaction pathways of the POD-like reaction. (e) Corresponding free energy diagrams of CeO_2 and Au/CeO_2 for the POD-like reaction.
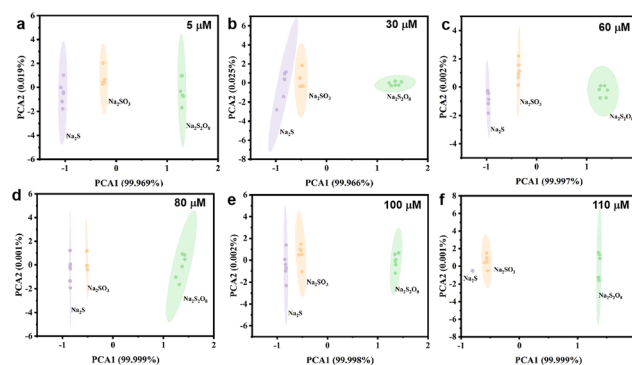
eV), indicating a greater likelihood of electron transfer within Au/CeO$_2$, thus enhancing the catalytic rate. Additionally, the density of states analysis (Fig. 5c) indicates that both CeO$_2$ and Au/CeO$_2$ exhibit metallic characteristics. Near the CeO$_2$ Fermi level, electron density is primarily due to Ce 3d and O 1s electrons, while in Au/CeO$_2$, Au 4f electrons influence the band near the Fermi level, offering spin polarization, indicative of the interaction between Au and CeO$_2$. The reaction pathways and energy profiles for the POD-like activity of Au/CeO$_2$ are shown in Fig. 5d and e. The adsorption energy of H$_2$O$_2$ on the Ce surface of Au/CeO$_2$ was −0.88 eV, which was lower than that on the Ce surface of CeO$_2$, suggesting that the Au-induced electron redistribution on the CeO$_2$ surface facilitates H$_2$O$_2$ adsorption. Subsequently, H$_2$O$_2$ decomposes into two OH* radicals, with Ce on Au/CeO$_2$ elevating the H$_2$O$_2$ decomposition energy by 0.05 eV. The subsequent OH* release on Ce atoms requires 0.15 eV less energy on Au/CeO$_2$ than on CeO$_2$, implying a higher propensity for Au/CeO$_2$ to generate active OH* species. Simultaneously, another OH* species on the Au/CeO$_2$ surface reacts with an adjacent H$^+$ to form H$_2$O adsorbed on the surface, accompanied by an energy increase of 0.22 eV, indicating that, thermodynamically, OH* to H$_2$O conversion is unfavorable. Finally, Au/CeO$_2$ is regenerated with an energy rise of 0.27 eV post-product formation. The DFT calculation data reveal that the Au/CeO$_2$ nanocatalyst exhibits exceptional POD-like activity, with the Au elements optimizing the electronic structure of CeO$_2$, thereby contributing to the enhanced overall catalytic efficiency. Furthermore, DFT demonstrates that Au can accept electrons from Ce^{3+} sites of CeO$_2$ and increase their Ce^{4+}/Ce^{3+} ratios, which improve the peroxidase-like catalytic activity of nanocomposite. Consequently, these results indicate that the Au/CeO$_2$ nanozyme exhibited superior nanozyme activity in decomposing H$_2$O$_2$ to ROS.

3.4 Responses of the colorimetric sensor array based on Au/CeO$_2$ to SCMs

Based on the distinct SCMs exhibiting significant effects on the reduction activity to oxTMB, a novel colorimetric sensor array was developed. To prove the feasibility of the colorimetric sensor array, three kinds of SCMs including Na$_2$S, Na$_2$SO$_3$ and Na$_2$S$_2$O$_8$ were chosen as examples. Notably, the presence of SCMs remarkably inhibited the UV-Vis absorption intensity of the [Au/CeO$_2$ + TMB/H$_2$O$_2$] reaction system, except for Na$_2$S$_2$O$_8$. When the various concentrations of Na$_2$S$_2$O$_8$ were added into the reaction system, the absorption intensities were enhanced, which could be ascribed to the process of further oxidation of TMB by +7 valence state. As a result, they were then further oxidized by Na$_2$S$_2$O$_8$. SCMs exhibited diverse reducing capabilities to oxTMB according to diverse sulfur valence states, which suggested that their diverse interaction effects on the peroxidase-like catalytic capability of Au/CeO$_2$ offered the prerequisite for their recognition. In this work, we selected Na$_2$S, Na$_2$SO$_3$, and Na$_2$S$_2$O$_8$ as detection targets. First, the signal range (5, 30, 60, 80, 100, and 110 μM) of the colorimetric sensor array to the above described SCMs was explored. If SCMs were present in the determination system, they could
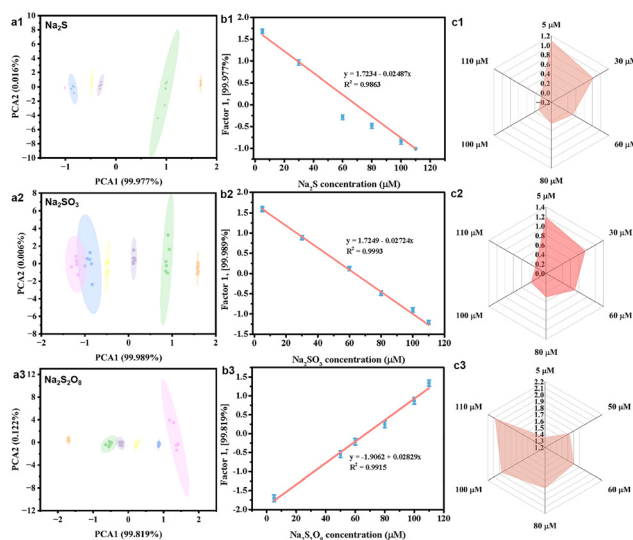
potentially decrease the TMBox signal by virtue of their inherent reducibility, rather than by directly disrupting with the oxidation of TMB. Interestingly, the reduction capability of oxTMB was contingent upon the valence state of the sulfur atom within the SCMs. As a result, the reduction ability of the three SCMs ranked in the following order of decreasing ability: Na$_2$S (−2) > Na$_2$SO$_3$ (+4) > Na$_2$S$_2$O$_8$ (+7). When three kinds of SCMs were added into the reaction system, they were accompanied by distinct colorimetric responses, directly demonstrating a one-to-one correspondence between each target SCM and its unique fingerprint spectrum. Thus, an accurate detection of the colorimetric fingerprint spectra was conducted, which proved the ability to distinguish diverse levels of the same SCMs. Fig. 6a–f show PCA distribution of the three kinds of SCMs at different concentrations. Interestingly, each figure showed a unique pattern of each SCMs, with three kinds of SCMs obviously separated from each other. When the concentration of SCMs increased, it could be seen that the relative scores of the three kinds of SCMs changed and gradually fared away from each other, suggesting the outstanding identification ability of the constructed colorimetric sensor array. The analytical performance of our sensor array for SCM detection increased with the increasing SCM concentration, and when the lowest concentration tended to be 5 M, the scores of the three SCMs was in a vital state, almost overlapping, suggesting that the colorimetric sensor array possessed the capability to recognize SCMs as low as 5 M. The above results demonstrated the feasibility of the actual application.

To further investigate the quantitative ability of the as-constructed colorimetric sensor array, the detection of each single SCM with diverse levels was analyzed by PCA. When diverse SCMs were added into the reaction system, they were accompanied by diverse colorimetric responses, suggesting that each analyst SCM possessed a one-to-one correspondence with its inherent fingerprint spectrum. A more accurate detection of the colorimetric fingerprint spectra was carried out with the help of PCA technology. As seen in Fig. 7, the colori-

Fig. 6 Canonical score plot for the identification of three kinds of SCMs at different concentrations ((a) 5 μM, (b) 30 μM, (c) 60 μM, (d) 80 μM, (e) 100 μM and (f) 110 μM).
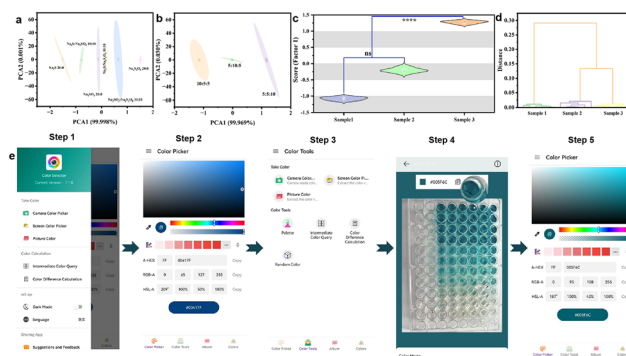
Fig. 7 PCA diagram of the colorimetric sensor array with diverse concentrations of SCMs ((a1) Na_2S, (a2) Na_2SO_3 and (a3) $Na_2S_2O_8$). (b1–b3) Plots of the discriminant factor 1 *vs.* the concentrations of SCMs. (c1–c3) Radar map of the colorimetric sensor array toward three kinds of SCMs. The y-axis scale represented the absorption intensity of oxTMB in the [Au/CeO_2 + TMB/H_2O_2] reaction system.

metric response from PCA of Na_2S, Na_2SO_3 and $Na_2S_2O_8$ were displayed based on their corresponding two discriminant factors accounting for approximately 100% of the variance. In each figure, the 36 colorimetric responses collected (6 concentrations × 6 replicates) obviously produced 6 clusters corresponding to each analyst SCM. From the 2D standard score plots, diverse levels of each sulfur-containing metal salt could be detected, suggesting that the as-constructed colorimetric sensor array could efficiently recognize different kinds of SCM at six levels by the PCA method. To explore the sensitivity of the as-developed colorimetric sensor array, the quantitative analytical performance for given SCMs was conducted. As depicted in the canonical score plot of 2D PCA (Fig. 7a1–a3), for each SCM, the 2D PCA plot of diverse concentrations endowed unique patterns, and these clusters were well separated from each other from 5 M to 110 M. Furthermore, we could see that clusters of diverse concentrations were regularly distributed in the plots, and the concentration exhibited an excellent correlation with factor 1. Since factor 2 was less than 5%, factor 1 could be utilized to quantify SCMs. As seen in Fig. 7b1–b3, factor 1 displayed an outstanding linear relationship with the concentrations of SCMs in the range of 5–110 μM. The above excellent linearity implied that the colorimetric sensor array possessed superior analytical performance and could also achieve sensitive determination of individual SCM. In addition, the radar plot in Fig. 7c1–c3 shows the comparison of the capability of each SCM to regulate the POD-like catalytic activity of Au/CeO_2. Compared with other previously reported detection methods (Table S1†), Au/CeO_2 exhibits comparable or better performance in SCM discrimination.

3.5 Discrimination of mixtures in real samples

Further, in order to investigate the detection and recognition capability of the as-developed colorimetric sensor array toward multiple mixtures, we utilized the binary mixtures of these SCMs ($Na_2S : Na_2SO_3 = 10 : 10$, $Na_2S : Na_2S_2O_8 = 10 : 10$ and $Na_2SO_3 : Na_2S_2O_8 = 10 : 10$; the total concentration was 20 μM) and ternary mixtures ($Na_2S : Na_2SO_3 : Na_2S_2O_8 = 10 : 5 : 5$, $5 : 10 : 5$, $5 : 5 : 10$; the total concentration was 20 μM) as analytes to conduct the test. As the data show in Fig. 8a and b, all of the binary mixtures or ternary mixtures were well discriminated against one another with no error or misclassifications in the reaction systems, suggesting the good performance of the colorimetric sensor array in distinguishing standard SCM sample mixtures and laying a great application potential for the determination of SCMs in actual samples. Meanwhile, the storage stability of the Au/CeO_2 nanozyme during storage was analyzed and is depicted in Fig. S3,† suggesting that POD-like catalytic effectiveness was above 95% after a long-storage duration of 30 days.

Real samples were differentiated utilizing PCA and hierarchical cluster analysis (HCA) to evaluate the potential application of the as-fabricated sensor array according to diverse SCM levels (Fig. 8c and d). Due to the use of bleach, SCMs became the main pollutants affecting the water quality. Water samples acquired from the Dalong lake were used as actual samples. Prior to the formal test, a 0.22 μm microporous membrane was employed to remove the suspended impurities in river water. Three SCMs with a final concentration of 30 μM were introduced into the samples for further analysis. PCA analysis of the fingerprint data was then conducted. As depicted in Fig. S4,† river water generated a unique colorimetric signal, while the clusters of three SCMs in river water displayed excellent separation without overlapping identifications due to the remarkable difference in SCM level. As seen in Fig. 8c, an obvious difference was exhibited in the violin chart score of discriminant factor 1 *vs.* the samples. Hierarchical cluster analysis (HCA) is a robust clustering strat-

Fig. 8 (a) Binary and (b) ternary sulfur-containing compound mixtures at different molar ratios, respectively. Plot of the factor 1 and HCA dendrogram *vs.* three environmental samples (c and d), respectively. (e) Smartphone sensing platform according to "Color Selector" APP software for SCM detection.

egy according to Euclidean distances; starting from a single sample, new clusters were produced by introducing the next most similar sample to the existing clusters until all of the samples are integrated into one cluster. Due to their high similarity, each group of samples was identified without any overlapping by HCA technology (Fig. 8d). The above result suggested that the colorimetric sensor array could be utilized in the SCM detection of environmental samples with good accuracy.

To meet the on-site application of the Au/CeO$_2$-based colorimetric sensor array for SCM determination, the idea of constructing an intelligent and convenient smartphone sensing platform according to "Color Selector" APP software that combined a colorimetric response was developed. As seen in Fig. 8e, the following five steps were conducted with the help of a smartphone from step 1 to step 5, and the operation procedure has been exhibited in detail. Finally, we hoped to successfully construct this smartphone-based simple and fast strategy for the on-site analysis of SCM types and their levels without the need for clumsy instruments and equipment and professional operators.

4. Conclusion

In conclusion, Au NPs as an electron bank promote charge redistribution on the surface of CeO$_2$. This process increases the ratio of Ce^{3+}/Ce^{4+}, facilitates the release of OH* and enhances the desorption of H$_2$O, thereby significantly improving the POD-like activity. Conversely, SCMs could significantly inhibit the signal response of the [Au/CeO$_2$ + TMB/H$_2$O$_2$] reaction system, resulting in noticeable color fading. Leveraging this different response mechanism, a simple, low-cost, robust and efficient visual colorimetric sensor array was constructed. Upon the addition of analytes such as SCMs into the reaction system, a unique fingerprint is generated, enabling the recognition and quantitative detection of different SCMs. Utilizing PCA technology, we successfully identified three kinds of SCMs at concentrations as low as 5 μM and also realized the recognition of differentiated mixtures of SCMs. Taken together, the as-established colorimetric sensor array was simple in nanozyme preparation, rapid in response, portable in operation procedures, and high in sensitivity, opening the way to its strength and promising potential in the field of on-site detection.

Data availability

The data that support the findings of this study are available from the corresponding author upon reasonable request.

Conflicts of interest

There are no conflicts to declare.

Acknowledgements

References

1 T. Y. Qi, S. Zhang, T. Li, L. Xing, S. L. An, Q. W. Li and L. D. Wang, *Environ. Sci. Technol.*, 2023, **57**, 15759.
2 L. Sacarescu, A. L. Chibac-Scutaru, G. Roman, G. Sacarescu and M. Simionescu, *Environ. Chem. Lett.*, 2023, **21**, 561–596.
3 W. J. Qin, L. Su, C. Yang, Y. H. Ma, H. J. Zhang and X. G. Chen, *J. Agric. Food Chem.*, 2014, **62**, 5827–5834.
4 H. Y. Zhang, S. H. Xue and G. Q. Feng, *Sens. Actuators, B*, 2016, **231**, 752–758.
5 Y. H. Yan, K. Zhang, H. Yu, H. J. Zhu, M. T. Sun, T. Hayat, A. Alsaedi and S. H. Wang, *Talanta*, 2017, **174**, 387–393.
6 S. Balasurya, A. Syed, A. M. Thomas, N. Marraiki, A. M. Elgorban, L. L. Raju and S. S. Khan, *Mater. Chem. Phys.*, 2021, **257**, 123789.
7 L. Yan, Q. S. Gu, W. L. Jiang, M. Tan, Z. K. Tan, G. J. Mao, F. Xu and C. Y. Li, *Anal. Chem.*, 2022, **94**, 5514–5520.
8 Y. X. Yu, G. L. Li, D. Wu, F. P. Zheng, X. L. Zhang, J. H. Liu, N. Hu, H. L. Wang and Y. N. Wu, *J. Agric. Food Chem.*, 2020, **68**, 876–883.
9 W. Zgagacz, R. Zakrzewski, K. Urbaniak, G. Chwatko and A. Nowicki, *J. Chromatogr. B:Anal. Technol. Biomed. Life Sci.*, 2020, **1157**, 122309.
10 I. S. Turan and F. A. Sozmen, *Sens. Actuators, B*, 2014, **201**, 13–18.
11 X. M. Dong, L. X. Sun, Z. W. Zhang, T. L. Zhu, J. Sun, J. Z. Gao, C. J. Dong, R. C. Wang, X. F. Gu and C. C. Zhao, *Sci. China: Chem.*, 2023, **66**, 1869–1876.
12 Y. M. Zuo, S. S. Wang, R. Z. Lin, G. L. Xiao, S. Chen, R. J. Zeng and H. Gu, *Talanta*, 2023, **256**, 124269.
13 N. L. Zhu, T. H. Deng, Y. N. Zuo, J. Sun, H. W. Liu, X. E. Zhao and S. Y. Zhu, *Spectrochim. Acta, Part A*, 2023, **295**, 122620.
14 F. Rahimi and M. Anbia, *Microchem. J.*, 2023, **190**, 108583.
15 Q. M. Zhong, R. R. Zhang, B. B. Yang, T. T. Tian, K. Zhang and B. H. Liu, *ACS Sens.*, 2022, **7**, 893–899.
16 O. Tinkov, P. Polishchuk, M. Matveieva, V. Grigorev, L. Grigoreva and Y. Porozov, *Mol. Inf.*, 2021, **40**, 2000209.
17 Z. Li, X. Zhang, H. R. Cheng, Z. Y. Gu, C. C. He, J. Wang, X. X. Shi, W. D. Na, T. X. Li and L. Tian, *Chem. Eng. J.*, 2024, **502**, 157904.
18 L. P. Luo, J. C. Zhuo, Y. N. Zhang, W. H. Zhang, W. Q. Su, J. Sun, Y. Z. Shen and J. L. Wang, *Environ. Sci. Technol.*, 2023, **57**, 13397–13407.
19 Z. W. Qiu, W. Duan, S. F. Cao, T. Zeng, T. Y. Zhao, J. K. Huang, X. Q. Lu and J. B. Zeng, *Environ. Sci. Technol.*, 2022, **56**, 1713–1723.
20 M. M. Bordbar, J. Tashkhourian and B. Hemmateenejad, *ACS Appl. Mater. Interfaces*, 2022, **14**, 8333–8342.

21 Z. L. Lu, N. Lu, Y. Xiao, Y. Q. Zhang, Z. S. Tang and M. Zhang, *ACS Appl. Mater. Interfaces*, 2022, **14**, 11156–11166.

22 M. X. Wu, H. Y. Chen, Y. Fan, S. T. Wang, Y. Hu, J. Liu, C. H. Shen, C. S. Zhou, H. Y. Fu and Y. B. She, *Food Chem.*, 2022, **372**, 131216.

23 Z. H. Qing, L. X. Zhu, X. X. Li, S. Yang, Z. Zou, J. R. Guo, Z. Cao and R. H. Yang, *Environ. Sci. Technol.*, 2017, **51**, 11884–11890.

24 C. M. Yang and H. J. Zhang, *Microchim. Acta*, 2023, **190**, 451.

25 L. Tian, Z. J. Huang, W. D. Na, Y. Y. Liu, S. Wang, Y. He, W. J. Cheng, T. Z. Huang, Z. Li and T. X. Li, *Nanoscale*, 2022, **14**, 15340–15347.

26 L. Tian, Z. J. Huang, X. H. Lu, T. J. Wang, W. J. Cheng, H. M. Yang, T. Z. Huang, T. X. Li and Z. Li, *Inorg. Chem.*, 2023, **62**, 1659–1666.

27 F. L. Wu, H. S. Wang, J. H. Lv, X. M. Shi, L. F. Wu and X. D. Niu, *Biosens. Bioelectron.*, 2023, **236**, 115417.

28 L. F. Wu, J. Y. Li, H. S. Wang, K. Y. Pan, X. M. Shi and X. D. Niu, *Adv. Funct. Mater.*, 2025, **35**, 2413154.

29 X. D. Niu, L. F. Wu, F. L. Wu, J. Q. Guan and H. S. Wang, *Biosens. Bioelectron.*, 2023, **238**, 115606.

30 Y. Y. Ma, Z. M. Tian, W. F. Zhai and Y. Q. Qu, *Nano Res.*, 2022, **15**, 10328–10342.

31 S. F. Zhang, H. Y. Ruan, Q. Xin, X. Y. Mu, H. Wang and X. D. Zhang, *Nanoscale*, 2023, **15**, 4408–4419.

32 H. S. Wang, F. L. Wu, L. F. Wu, J. Q. Guan and X. D. Niu, *J. Hazard. Mater.*, 2023, **456**, 131643.

33 L. Wei, Y. X. Liu, H. X. Dai, S. P. Cui, C. Wang, H. C. Hsi, E. H. Duan, Y. Peng and J. G. Deng, *Appl. Catal., B*, 2022, **304**, 120939.

34 Z. H. Zhang, Z. H. Yu, K. Feng and B. H. Yan, *Appl. Catal., B*, 2022, **317**, 121800.

35 F. Jiang, S. S. Wang, B. Liu, J. Liu, L. Wang, Y. Xiao, Y. B. Xu and X. H. Liu, *ACS Catal.*, 2020, **10**, 11493–11509.

36 F. X. Cao, Z. Y. Song, Z. M. Zhang, Y. S. Xiao, M. K. Zhang, X. Hu, Z. W. Liu and Y. Q. Qu, *ACS Appl. Mater. Interfaces*, 2021, **13**, 24957–24965.

37 M. Wang, M. Shen, X. X. Jin, J. J. Tian, M. L. Li, Y. J. Zhou, L. X. Zhang, Y. S. Li and J. L. Shi, *ACS Catal.*, 2019, **9**, 4573–4581.

38 M. Soh, D.-W. Kang, H.-G. Jeong, D. Kim, D. Y. Kim, W. Yang, C. Song, S. Baik, I.-Y. Choi, S.-K. Ki, H. J. Kwon, T. Kim, C. K. Kim, S.-H. Lee and T. Hyeon, *Angew. Chem., Int. Ed.*, 2017, **56**, 11399–11403.

39 Z. Y. Huang, M. Liao, S. F. Zhang, L. X. Wang, M. C. Gao, Z. Y. Luo, T. T. Isimjan, B. Wang and X. L. Yang, *J. Energy Chem.*, 2024, **90**, 244–252.

40 H. Y. Lin, J. H. Wang, S. Q. Xu, Q. Zhang, Y. Q. Cheng, D. Han, H. T. Wang and K. Zhuo, *ACS Appl. Nano Mater.*, 2022, **5**, 14311–14319.

41 V. Zólyomi and J. Kürti, *Phys. Rev. B*, 2004, **70**, 8.